UNIVERSITY OF AMSTERDAM

UvA-DARE (Digital Academic Repository)

The Metallicity and Dust Content of a Redshift 5 Gamma-Ray Burst Host Galaxy

Sparre, M.; Hartoog, O.E.; Krühler, T.; Fynbo, J.P.U.; Watson, D.J.; Wiersema, K.; D'Elia, V.; Zafar, T.; Afonso, P.M.J.; Covino, S.; de Ugarte Postigo, A.; Flores, H.; Goldoni, P.; Greiner, J.; Hjorth, J.; Jakobsson, P.; Kaper, L.; Klose, S.; Levan, A.J.; Malesani, D.; Milvang-Jensen, B.; Nardini, M.; Piranomonte, S.; Sollerman, J.; Sánchez-Ramírez, R.; Schulze, S.; Tanvir, N.R.; Vergani, S.D.; Wijers, R.A.M.J.

DOI
10.1088/0004-637X/785/2/150

Publication date
2014

Document Version
Final published version

Published in
Astrophysical Journal

Link to publication

Citation for published version (APA):
Sparre, M., Hartoog, O. E., Krühler, T., Fynbo, J. P. U., Watson, D. J., Wiersema, K., D'Elia, V., Zafar, T., Afonso, P. M. J., Covino, S., de Ugarte Postigo, A., Flores, H., Goldoni, P., Greiner, J., Hjorth, J., Jakobsson, P., Kaper, L., Klose, S., Levan, A. J., ... Wijers, R. A. M. J. (2014). The Metallicity and Dust Content of a Redshift 5 Gamma-Ray Burst Host Galaxy. *Astrophysical Journal*, *785*(2), 150. https://doi.org/10.1088/0004-637X/785/2/150

General rights
It is not permitted to download or to forward/distribute the text or part of it without the consent of the author(s) and/or copyright holder(s), other than for strictly personal, individual use, unless the work is under an open content license (like Creative Commons).

Disclaimer/Complaints regulations
If you believe that digital publication of certain material infringes any of your rights or (privacy) interests, please let the Library know, stating your reasons. In case of a legitimate complaint, the Library will make the material inaccessible and/or remove it from the website. Please Ask the Library: https://uba.uva.nl/en/contact, or a letter to: Library of the University of Amsterdam, Secretariat, P.O. Box 19185, 1000 GD Amsterdam, The Netherlands. You will be contacted as soon as possible.

UvA-DARE is a service provided by the library of the University of Amsterdam (https://dare.uva.nl)

Download date:10 Oct 2026

The Astrophysical Journal, 785:150 (12pp), 2014 April 20 doi:10.1088/0004-637X/785/2/150
© 2014. The American Astronomical Society. All rights reserved. Printed in the U.S.A.

THE METALLICITY AND DUST CONTENT OF A REDSHIFT 5 GAMMA-RAY BURST HOST GALAXY*

M. Sparre[1], O. E. Hartoog[2], T. Krühler[1,3], J. P. U. Fynbo[1], D. J. Watson[1], K. Wiersema[4], V. D'Elia[5,6], T. Zafar[7], P. M. J. Afonso[8], S. Covino[9], A. de Ugarte Postigo[1,10], H. Flores[11], P. Goldoni[12], J. Greiner[13], J. Hjorth[1], P. Jakobsson[14], L. Kaper[2], S. Klose[15], A. J. Levan[16], D. Malesani[1], B. Milvang-Jensen[1], M. Nardini[17], S. Piranomonte[18], J. Sollerman[19], R. Sánchez-Ramírez[10], S. Schulze[20,21], N. R. Tanvir[4], S. D. Vergani[9,11], and R. A. M. J. Wijers[2]

[1] Dark Cosmology Centre, Niels Bohr Institute, University of Copenhagen, Juliane Maries Vej 30, 2100 Copenhagen, Denmark; sparre@dark-cosmology.dk
[2] Anton Pannekoek Institute for Astronomy, University of Amsterdam, Science Park 904, 1098 XH, Amsterdam
[3] European Southern Observatory, Alonso de Córdova 3107, Vitacura, Casilla 19001, Santiago 19, Chile
[4] Department of Physics and Astronomy, University of Leicester, University Road, Leicester, LE1 7RH, UK
[5] INAF/Rome Astronomical Observatory, via Frascati 33, I-00040 Monteporzio Catone (Roma), Italy
[6] ASI Science Data Centre, Via Galileo Galilei, I-00044 Frascati (Roma), Italy
[7] European Southern Observatory, Karl-Schwarzschild-Strasse 2, D-85748 Garching, Germany
[8] Physics and Astronomy Department, American River College, 4700 College Oak Drive, Sacramento, CA 95841, USA
[9] INAF, Osservatorio Astronomico di Brera, via E. Bianchi 46, I-23807 Merate (LC), Italy
[10] Instituto de Astrofísica de Andalucía, CSIC, Glorieta de la Astronomía s/n, E-18008 Granada, Spain
[11] Laboratoire GEPI, Observatoire de Paris, CNRS-UMR8111, Universite Paris Diderot 5 place Jules Janssen, F-92195 Meudon, France
[12] APC, Astroparticule et Cosmologie, Universite Paris Diderot, CNRS/IN2P3, CEA/Irfu, Observatoire de Paris, Sorbonne Paris Cité, 10, Rue Alice Domon et Léonie Duquet, F-75205 Paris, Cedex 13, France
[13] Max-Planck-Institut für extraterrestrische Physik, Giessenbachstraße, D-85748 Garching, Germany
[14] Centre for Astrophysics and Cosmology, Science Institute, University of Iceland, Dunhagi 5, IS-107 Reykjavik, Iceland
[15] Thüringer Landessternwarte Tautenburg, Sternwarte 5, D-07778 Tautenburg, Germany
[16] Department of Physics, University of Warwick, Coventry CV4 7AL, UK
[17] Università degli studi di Milano-Bicocca, Piazza della Scienza 3, I-20126 Milano, Italy
[18] INAF-Osservatorio Astronomico di Roma, Via Frascati 33, I-00040 Monte Porzio Catone, Roma, Italy
[19] Oskar Klein Centre, Department of Astronomy, AlbaNova, Stockholm University, SE-106 91 Stockholm, Sweden
[20] Instituto de Astrofísica, Facultad de Física, Pontificia Universidad Católica de Chile, Casilla 306, Santiago 22, Chile
[21] Millennium Center for Supernova Science, Camino del Observatorio 1515, Las Condes, Chile
Received 2013 September 12; accepted 2014 March 10; published 2014 April 4

ABSTRACT

Observations of the afterglows of long gamma-ray bursts (GRBs) allow the study of star-forming galaxies across most of cosmic history. Here we present observations of GRB 111008A, from which we can measure metallicity, chemical abundance patterns, dust-to-metals ratio (DTM), and extinction of the GRB host galaxy at $z = 5.0$. The host absorption system is a damped Lyα absorber with a very large neutral hydrogen column density of $\log N(\mathrm{H\,I})/\mathrm{cm}^{-2} = 22.30 \pm 0.06$ and a metallicity of $[\mathrm{S/H}] = -1.70 \pm 0.10$. It is the highest-redshift GRB with such a precise metallicity measurement. The presence of fine-structure lines confirms the $z = 5.0$ system as the GRB host galaxy and makes this the highest redshift where Fe II fine-structure lines have been detected. The afterglow is mildly reddened with $A_V = 0.11 \pm 0.04$ mag, and the host galaxy has a DTM that is consistent with being equal to or lower than typical values in the Local Group.

Key words: dust, extinction – galaxies: high-redshift – gamma-ray burst: individual (GRB 111008A)

Online-only material: color figures

1. INTRODUCTION

The study of gamma-ray bursts (GRBs) has an impact on a wide range of topics in astrophysics. It is now well established that long-duration GRBs originate from the collapse of massive stars (e.g., Galama et al. 1998; Hjorth et al. 2003; Stanek et al. 2003; Modjaz et al. 2006; Campana et al. 2006; Sparre et al. 2011; Berger et al. 2011; Hjorth & Bloom 2012; Xu et al. 2013), although we have yet to elucidate the detailed nature of the progenitor systems.

Spectroscopy of GRB afterglows requires the most advanced and largest ground-based optical to near-infrared (NIR) telescopes, especially when these events occur at high redshift, since the source is weaker and the rest-frame UV absorption lines we detect are shifted to longer wavelengths. GRB afterglows can probe star-forming regions out to redshifts of $z = 8$–9 (Tanvir et al. 2009; Salvaterra et al. 2009; Cucchiara et al. 2011) and allow us to study galaxies in the early universe that would normally have been too faint to be detected (Tanvir et al. 2012; Basa et al. 2012). In some cases it is possible to determine column densities of both H I and metals in their host galaxies and hence calculate abundances for a wide range of chemical elements (e.g., Fynbo et al. 2006; Savaglio 2006; Prochaska et al. 2007b; Ledoux et al. 2009; D'Elia et al. 2010; Thöne et al. 2013).

Observational selection effects restrict the samples of GRBs for which chemical enrichment can be probed by this means. For many GRBs, even when spectroscopy is obtained, it proves insufficient to probe the rest-frame UV due to unfortunate redshifts that leave the relevant transitions (in particular H I) out of the observable range. In other cases, dust extinction within the host galaxies (the likely explanation for many "dark" bursts; see Jakobsson et al. 2004; Perley et al. 2009; Krühler et al. 2011) makes the afterglows too faint for useful spectroscopy. Therefore, the sample of bursts with afterglow spectroscopy is not representative for all GRBs (e.g., Fynbo et al. 2009; Krühler et al. 2013).

With observations of GRB afterglows one can hope to obtain the imprints in the interstellar medium (ISM) of chemical enrichment from core-collapse supernovae (SNe), which are

* Based on observations carried out under ESO program ID 088.A-0051(B) and 091.A-0703(A).

believed to dominate the metal production for very young systems (e.g., Matteucci & Greggio 1986). The signature of such a chemical enrichment profile is an overabundance of α elements as seen in metal-poor stars in the Local Group and in $z > 4$ damped Lyα absorbers (DLAs)[22] (e.g., Tolstoy 2011; Rafelski et al. 2012).

The aim of this article is to study the metal and dust properties of the host galaxy of GRB 111008A at $z = 5.0$, which provides a rare opportunity of measuring such characteristics for a high-redshift star-forming galaxy. The paper is structured as follows. In Section 2, we present our observations, in Section 3, we determine the metallicity of the host galaxy, and we also discuss the presence and strength of fine-structure lines. In Section 4, we describe the spectral energy distribution (SED) of the NIR-to-X-ray data. In Section 5, we investigate an intervening DLA at $z = 4.6$, in Section 6, we present an attempt to identify the intervening absorber and the GRB host galaxy in emission, and in Section 7, we study the amount of dust and metals in the host galaxy.

For the cosmological calculations we assume a ΛCDM-universe with $\Omega_\Lambda = 0.73$, $\Omega_m = 0.27$, and $h_0 = 0.71$. We use 1σ error bars and 2σ upper and lower limits.

2. OBSERVATIONS

GRB 111008A was discovered by *Swift*/BAT (Saxton et al. 2011) with a duration of $T_{90} = 63.46 \pm 2.19$ s (Baumgartner et al. 2011). An X-ray counterpart was subsequently discovered with *Swift*/XRT (Beardmore et al. 2011), and the optical counterpart was later observed using several instruments (Levan et al. 2011a; Xu et al. 2011; Nardini et al. 2011) before a spectroscopic redshift of $z = 5.0$ was identified with Gemini/GMOS (Levan et al. 2011b). This was later confirmed with VLT/X-shooter, and an intervening absorber at $z = 4.6$ was also identified (Wiersema et al. 2011). The details of our observations are given below.

2.1. X-shooter Spectroscopy

We obtained optical/NIR spectroscopy of the afterglow of GRB 111008A with X-shooter (Vernet et al. 2011) mounted at UT2 of the European Southern Observatory's (ESO) Very Large Telescope (VLT). Our spectrum covers the wavelength range of 3000–24, 800 Å and was taken simultaneously in three arms (UVB, VIS, and NIR) using slit widths of 1.″0, 0.″9, and 0.″9 for UVB, VIS, and NIR, respectively. The nominal values of the spectral resolution for these configurations are $R = \lambda/\Delta\lambda(\mathrm{FWHM}) = 5100$, 8800, and 5100, respectively.

X-shooter spectroscopy started on 2011 October 9 05:55:49 UT, 8.52 hr after the trigger (Wiersema et al. 2011), and was performed at a median seeing of 1.″1 and an average airmass of 1.04. We obtained five exposures with a total integration time of 8775 s in the UVB and VIS arm, and 14 exposures (total exposure of 8400 s) in the NIR arm. A second X-shooter epoch was obtained the following night (starting 20.10 hr after the trigger, on 2011 October 10 04:24:25 UT) with a total integration time of 7897 s in UVB and VIS and 7200 s in NIR. All frames were reduced separately using the ESO X-shooter pipeline `v2.0.0` (Modigliani et al. 2010), and the resulting frames were stacked per night with a weighting based on the signal-to-noise ratio (S/N) of the afterglow detection. Flux calibration was performed against the spectrophotometric standard GD71 observed starting on 2011 October 8 08:58:03 UT. The one-dimensional spectra were extracted using optimal, variance weighting (Horne 1986). The optimal extraction and the stacking of science frames were done by a custom-made script developed for this purpose. Unless stated explicitly (as in Section 3.2), we base our results on the combined spectrum of the first night of X-shooter observations, because of the superior S/N.

The complete VIS and NIR part of the X-shooter spectrum and the measured absorption lines are shown in Appendix B.

2.2. GMOS Spectroscopy

We observed the afterglow of GRB 111008A using the Gemini Multi-Object Spectrograph (GMOS) on the Gemini-South telescope.[23] After identification of the optical afterglow (Levan et al. 2011b), a series of four exposures with a total integration time of 2400 s were taken, using the R400 grism and a 1.″0 slit width, starting at 2011 November 9 03:29:29.7 UT.

The four exposures were taken using dithers in both the dispersion direction (50 Å) and the spatial direction (along the slit) to sample over the chip gaps and regions affected by amplifier location. We reduced the data using the Gemini GMOS reduction package (version 1.11) within IRAF, combining the four exposures after extraction, resulting in a wavelength range of ∼3900–8170 Å. The resolution of the exposures is $R \sim 870$.

2.3. GROND Photometry

The Gamma-Ray burst Optical/Near-infrared Detector (GROND; Greiner et al. 2008) at the 2.2 m MPI/ESO telescope on the La Silla Observatory started photometric observations of the field of GRB 111008A on 2011 November 9, 04:38:45 UT, which is 6.43 hr after the BAT trigger. Simultaneous photometry in seven optical/NIR filters (similar to the Sloan Digital Sky Survey (SDSS) $g'r'i'z'$ and the Two Micron All Sky Survey (2MASS) JHK_s bands) was obtained continuously until 09:02:10 UT. GROND data were reduced in a standard fashion (Krühler et al. 2008), using a custom pipeline written in IRAF/pyraf. The photometric solution was obtained by using magnitudes of stars in an SDSS field (Aihara et al. 2011) observed directly after the GRB field under photometric conditions in the case of the $g'r'i'z'$ filters, and via the magnitudes of 2MASS stars in JHK_s (Skrutskie et al. 2006). Based on the scatter of individual calibration stars, we estimate the absolute accuracy of our photometry to be 4% in $g'r'i'z'$, 5% in J/H, and 8% in K_s.

3. THE GRB HOST ABSORBER

In Figure 1, we provide an excerpt of the VIS spectrum (from X-shooter), which has been rebinned by a factor of four for graphical reasons. The VIS spectrum exhibits a very strong DLA, which is identified as absorption within the host galaxy, providing the redshift of the GRB. The corresponding Lyβ line is also detected. Shown in red is a Voigt-profile fit to the DLA and Lyβ lines corresponding to an H I column density of $\log N/\mathrm{cm}^{-2} = 22.30 \pm 0.06$. Also seen in the VIS spectrum is an intervening DLA at redshift $z = 4.6$, which will be discussed in Section 5. When determining the H I column density of the two absorbers, we fix the redshift to the value measured from the metal line fit (see Section 3.1), and next we determine $\log N(\mathrm{H\,I})$

[22] DLA (damped Lyα absorber): a sight line absorber with $\log N(\mathrm{H\,I})/\mathrm{cm}^{-2} > 20.30$ (Wolfe et al. 2005).

[23] For an overview of Gemini afterglow spectra, see http://grbspecdb.ucolick.org/.

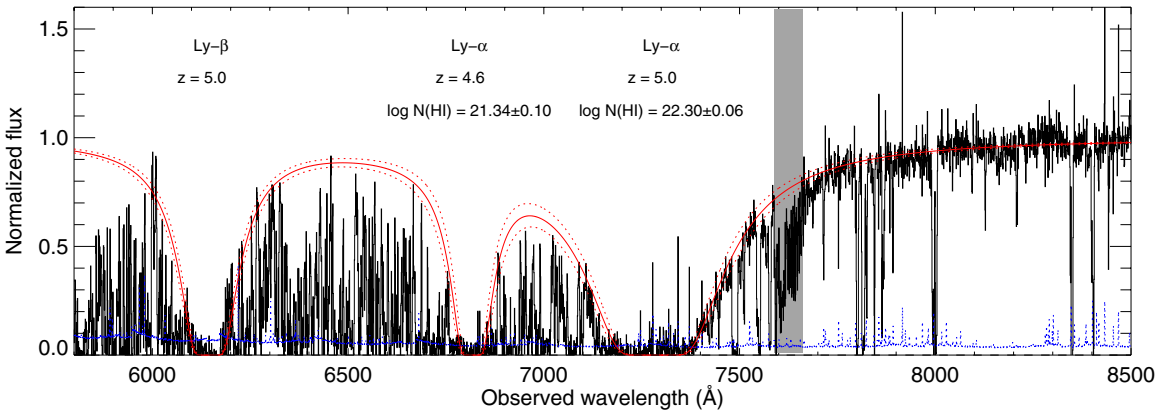

Figure 1. Excerpt of the VIS spectrum showing absorption from Lyα and Lyβ of the host galaxy of GRB 111008A ($z = 5.0$) and Lyα of the strong intervening system at $z = 4.6$. The red line displays a Voigt-profile fit to the DLAs Lyα and Lyβ lines. The dashed line shows the 1σ error on the fit result, and the dotted line shows the error spectrum. The shaded gray indicates a region with strong telluric contamination.

(A color version of this figure is available in the online journal.)

subjectively by looking at the red wing of the Lyα and Lyβ profiles. The error reflects what we consider the acceptable range of possible column densities.

3.1. The Chemical Composition

To determine abundances of the atomic ground-state levels, we proceed with Voigt-profile fitting of the X-shooter spectrum.[24] We find that a model with two absorption components per transition is sufficient to fit the low-ionization absorption lines. The spectral resolution is set to the nominal values from the X-shooter manual (a velocity resolution of 34 km s^{-1} for VIS and 57 km s^{-1} for NIR, both FWHM). The choice of spectral resolution and the placement of the continuum are unlikely to change the logarithm of the column densities by more than 0.15 dex.

The two Voigt profiles have Doppler parameters of $b = 20.9 \pm 2.3$ km s^{-1} and $b = 27.7 \pm 2.3$ km s^{-1} and redshifts of 4.99005 ± 0.00007 and 4.99142 ± 0.00006, respectively (these are the precise measured redshifts for the two absorption components in the GRB host absorption system; for brevity we will refer to the GRB host redshift as 5.0 in the remaining parts of the article). We linked the Doppler parameters for the different atoms assuming turbulent broadening, which is a standard procedure for low-ionization absorption lines (Wolfe et al. 2005). We also linked the redshifts for each of the absorption components. Figure 2 shows the fit of the line transitions for Si II, S II, Cr II, Mn II, Fe II, Ni II, and Zn II.

The derived metal column densities for the sum of the two components are provided in Table 1. Note that this table also includes the column densities in excited levels (from Section 3.2). The best-determined column densities are Ni and Fe, since they are constrained by relatively weak transitions (Ni II λ1370 and Fe II λ1611) located in regions with a good S/N. For Fe II λ1611 the measured spectrum exhibits excess absorption (at $\simeq -15$ km s^{-1}) compared to the fit model. It is unclear whether this feature is due to an additional absorption component or a systematic error. If it is due to an additional absorption component, our column density of Fe II is slightly underestimated by $\lesssim$15%.

For the S II λ1253 transition, the S/N is also high, and the measurement is reliable even though this line is mildly saturated (see a detailed explanation in Appendix A). For Cr II, we were able to estimate the column density with Cr II λ2056 and Cr II λ2066.

3.1.1. Systematic Errors in the Fitting of Si, Mn, and Zn for the GRB Host

The estimate of the column density of Si is unreliable because it is estimated using two lines, where one of them is saturated (Si II λ1526) and the other is affected by a sky-line (Si II λ1808). We therefore only report a lower limit on the column density based on Si II λ1808. The estimated column density of Zn is also uncertain, since the blue component of the Zn II λ2062 transition is blended with Cr II λ2062.[25] Visually, the model fit of Mn II λ2606 does not convincingly fit the data (and $\chi^2/\mathrm{dof} = 4.55$ for this transition, which also indicates a bad fit), so our measurement of the Mn column density is unreliable.

In the last column of Table 1, these caveats are summarized. Since the derived column densities of Si, Mn, and Zn are unreliable, we will not draw any conclusions based on them.

3.2. Fine-structure Lines

At $z = 5.0$ we detect lines that arise from the following fine-structure and metastable levels: C II $^2P^\circ_{3/2}$ (**), O I $^3P^\circ_0$ (**), Si II $^2P^\circ_{3/2}$ (*), Fe II ($^6D_{7/2}$, $^6D_{5/2}$, $^6D_{1/2}$, $^4F_{9/2}$, $^4F_{5/2}$, $^4D_{7/2}$, $^4D_{5/2}$, $^4D_{3/2}$), and Ni II $^4F_{9/2}$. To date, this is the highest redshift at which lines of these excited states of Fe II and Ni II have been detected. Lines from these excited levels are expected in GRB host galaxies and often detected at lower redshifts, but due to their relative weakness, the S/N required to detect them is often not reached at high redshift. Lines from Fe II $^6D_{3/2}$ and $^4F_{7/2}$ are not clearly detected due to their unfortunate placing either outside atmospheric windows or because they are severely affected by telluric lines. The Gemini/GMOS and X-shooter data together cover a time span from 5 to 40 hr after the burst (observer frame), making the data set suited to look for variability in lines from excited levels. Line variability is expected, because the fine-structure and metastable levels are populated through indirect UV-pumping by the GRB afterglow (Prochaska et al. 2006; Vreeswijk et al. 2007). The lines from

[24] The absorption lines are fitted with VPFIT version 10.0: http://www.ast.cam.ac.uk/~rfc/vpfit.html.

[25] In our estimate, we assumed that $\log N/\mathrm{cm}^{-2}$ for the blue component of Zn is 0.1 dex lower than for the red component, since this is what we see for Ni II λ1370.

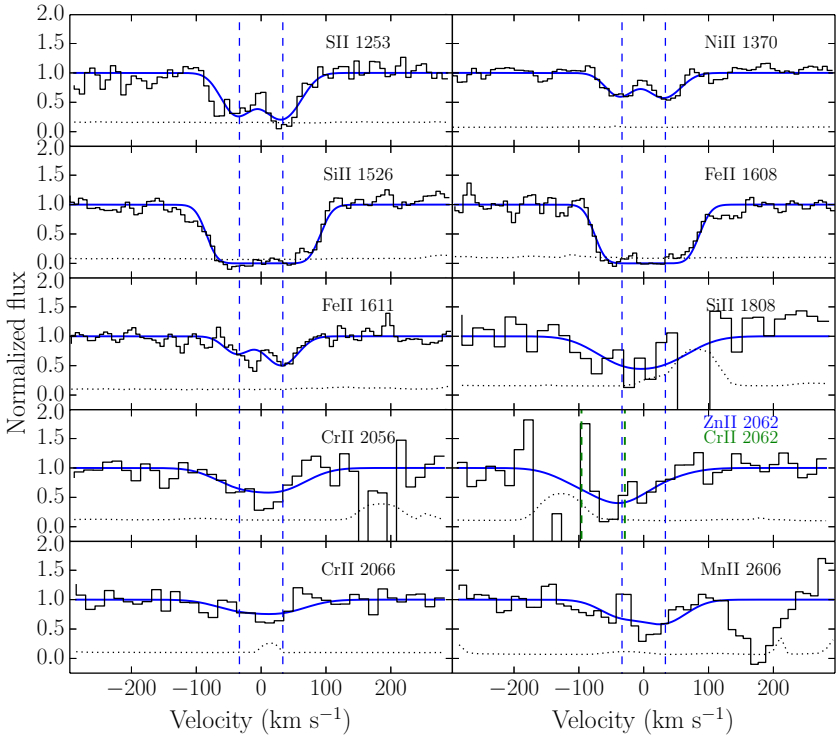

Figure 2. Fitted absorption lines from the host galaxy at $z = 5.0$. The black line is the spectrum, the blue line is the fitting model, and the dotted line is the error spectrum. The centers of the absorption line components are marked with dashed vertical lines.

(A color version of this figure is available in the online journal.)

Table 1
The Abundance Pattern of the Transitions (Including Excited Levels) in the GRB 111008A Host Galaxy and for the Intervening Absorber

Element	$\log N(X)/\mathrm{cm}^{-2}$	$[X/\mathrm{H}]$	Lines Used in Fit	Note
	GRB host			
H	22.30 ± 0.06	...	Lyα, Lyβ	
Si	>15.86 (2σ)	> -1.96 (2σ)	Si II λ1808, Si II λ1526	Lines are saturated
S	15.71 ± 0.09	-1.70 ± 0.10	S II λ1253	
Cr	14.17 ± 0.09	-1.76 ± 0.11	Cr II λ2056, Cr II λ2062, Cr II λ2066	
Mn	13.72 ± 0.08	-2.01 ± 0.10	Mn II λ2606	Fit is not convincing
Fe	16.05 ± 0.05	-1.74 ± 0.08	Fe II λ1608, Fe II λ1611	
Ni	14.89 ± 0.18	-1.64 ± 0.19	Ni II λ1370	
Zn	13.28 ± 0.21	-1.58 ± 0.21	Zn II λ2062	Blended with Cr II λ2062
	$z = 4.6$ system			
H	21.34 ± 0.10	...	Lyα	
Si	>14.91 (2σ)	>-2.15 (2σ)	Si II λ1526	Lines are saturated
Fe	15.23 ± 0.15	-1.61 ± 0.17	Fe II λ1608, Fe II λ1611	
Ni	14.23 ± 0.08	-1.33 ± 0.12	Ni II λ1370, Ni II λ1741	

Notes. Lower limits are at a 2σ level. Abundances from the solar photosphere from Asplund et al. (2009) were used as reference.

excited states and their corresponding ground states that fall in the spectral region covered by both GMOS and X-shooter are all likely saturated; therefore, we compare their rest-frame equivalent width ($\mathrm{EW_{rest}}$); see Table 2. The values of $\mathrm{EW_{rest}}$ for the lines and line blends (including both resonance and excited states) at the top of Table 2 are constant in time within 2σ, except Si II* λ1309. However, the temporal variation of this line does not match that of the stronger Si II* λ1264 lines, which it should follow. One possible explanation for this is that the uncertainty on Si II* λ1309 is probably underestimated, especially in the last epoch.

The lines from the excited states of Fe II and Ni II, which are not covered by GMOS, are weaker (and not saturated) and can be fitted with Voigt profiles in the X-shooter spectra. We couple z and b and fit one component to the lines of these levels in the first X-shooter epoch. The redshift is consistent with the red component of the resonance lines. With the obtained z and b kept fixed, this fit is repeated on the second X-shooter epoch, though none of the lines are clearly detected. Therefore, we report 2σ upper limits on the population of these excited states (see Table 2). Here again we see no evidence for time variation for an individual excited state. We note that the upper limits on the derived column densities are larger in the second X-shooter epoch compared to the first X-shooter epoch, since the S/N is lower in the second epoch.

From the measurements on the first X-shooter spectrum we conclude that the column density of the metastable level Fe II $^4F_{9/2}$ is, despite its higher energy, as high as that of the first

Table 2
Measurements of Lines from Fine-structure and Metastable States at the Host-galaxy Redshift ($z = 5.0$) in Three Different Epochs

Time of Mid Exposure[a] (hr)		6.27 GMOS	10.15 X-shooter 2011 November 9	34.82 X-shooter 2011 November 10
Ion	Line (Blend)	EW_{rest} (Å) of Saturated Lines and Blends		
C II + C II*	λ1334 + λ1335	2.05 ± 0.33	1.94 ± 0.04	1.77 ± 0.12
O I	λ1302	1.02 ± 0.02	1.05 ± 0.03	0.93 ± 0.05
O I**	λ1306	0.62 ± 0.17	0.36 ± 0.03	0.42 ± 0.07
S II + Si II	λ1259 + λ1260	1.58 ± 0.03	1.64 ± 0.03	1.79 ± 0.14
Si II*	λ1264 + λ1265	1.15 ± 0.03	1.05 ± 0.03	1.12 ± 0.10
Si II*	λ1309	0.37 ± 0.03	0.40 ± 0.02	0.14 ± 0.05
Ion	Level	Column Densities $\log N(X)/\mathrm{cm}^{-2}$ from Line Fits		
Fe II	$^6D_{9/2}$ (ground)	[b]	15.72 ± 0.08[c]	<16.14
	$^6D_{7/2}$	[b]	14.63 ± 0.06	<14.74
	$^6D_{5/2}$	[b]	14.53 ± 0.07	<14.80
	$^6D_{1/2}$	[b]	13.71 ± 0.11	...
	$^4F_{9/2}$	[b]	14.66 ± 0.12	...
	$^4F_{5/2}$	[b]	14.09 ± 0.24	...
	$^4D_{7/2}$	[b]	13.66 ± 0.05	<13.68
	$^4D_{5/2}$	[b]	13.34 ± 0.08	<13.91
	$^4D_{3/2}$	[b]	12.95 ± 0.12	<14.01
Ni II	$^2D_{5/2}$ (ground)	14.62 ± 0.77	14.34 ± 0.05	14.33 ± 0.20
	$^4F_{9/2}$	[b]	14.73 ± 0.26	...

Notes. The limits are at a 2σ confidence level.
[a] Time since burst. Not taking into account that we use an average spectrum weighted by the S/N of a fading source.
[b] All lines are outside the spectral range of GMOS.
[c] This is only the red component, which coincides with the position of the fine-structure lines.

excited state Fe II $^6D_{7/2}$ and that of all other, lower energy Fe II fine-structure states. Furthermore, Ni II $^4F_{9/2}$ is more populated than the Ni II ground state. This situation is typically the result of population by indirect radiative pumping. The Ni II $^4F_{9/2}$ population is expected to peak much later than the Fe II fine-structure states (after ∼2–10 hr post-burst in the rest frame, depending on light curve shape; see also Hartoog et al. 2013), which is consistent with our time of observations. Although a detailed model of the excitation has not been carried out in this paper, and despite the fact that we do not have evidence for variability in individual lines, our observations are consistent with the UV-pumping scenario, which confirms the $z = 5.0$ DLA as the host galaxy.

4. DETERMINING THE DUST EXTINCTION

We retrieved the X-ray spectrum of the afterglow of GRB 111008A from the *Swift*/XRT repository (Evans et al. 2007, 2009) and fit it together with the GROND broadband photometry in a standard manner (see, e.g., Krühler et al. 2013, for details). The fit is shown in Figure 3. We use synchrotron emission models, reddened by extinction laws from the Local Group (Pei 1992), and fit them to the available data. The absorption of soft X-rays is modeled with two absorbers at solar metallicity, one in the Galaxy (Kalberla et al. 2005; see also Willingale et al. 2013) and the other at the GRB redshift. The fit is performed with data at a mean photon arrival time of 35 ks after the trigger. AB magnitudes of the afterglow at this epoch in the different filters are $g' > 25.5$ mag, $r' = 23.11 \pm 0.07$ mag, $i' = 21.33 \pm 0.05$ mag, $z' = 20.37 \pm 0.05$ mag, $J = 19.91 \pm 0.06$ mag, $H = 19.72 \pm 0.06$ mag, $K_s = 19.62 \pm 0.10$ mag. We note that the $g'r'i'$ band data are not part of the fit, because they are located blueward of the Lyα transition. For the z' filter, the strong absorption lines from the GRB-DLA and strong intervening system reduce the observed flux significantly. We use the X-shooter spectrum to estimate their effect on the z'-band measurement and find that the continuum emission is approximately $7\% \pm 1\%$ above what is measured with GROND. This correction factor is applied in the following. The effect on the JHK_s magnitudes is $\lesssim 4\%$.

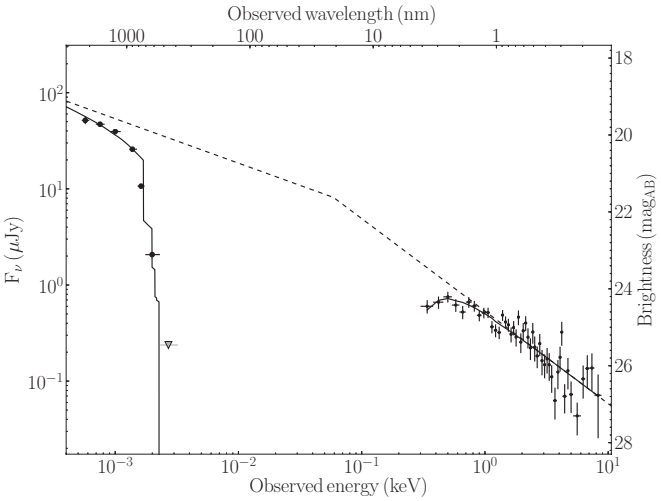

Figure 3. NIR-to-X-ray SED and model for the afterglow of GRB 111008A at an observed time of 35 ks after the GRB trigger. GROND photometry and the g' band upper limit are shown in larger black circles and a gray downward triangle, respectively. *Swift*/XRT X-ray data are plotted in smaller black dots. The best-fit model including gas and dust absorption is shown with solid lines, while the dashed line illustrates the underlying synchrotron emission. X-ray data have been binned to yield an S/N of at least eight to enhance clarity. The $g'r'i'$ band photometry is not fitted, because these filters are located or extend blueward of the Lyα transition.

The data are well fitted ($\chi^2 = 1.6$ in the optical/NIR, and Cash-statistic = 385 in the X-ray energy range, for a total of 362 dof) with a broken power law with a low-energy spectral index $\beta_1 = 0.46 \pm 0.06$ and a small amount of reddening in an

SMC-like (Small Magellanic Cloud) extinction law ($E_{B-V} = 0.037 \pm 0.012$ mag, corresponding to a visual extinction of $A_V = 0.11 \pm 0.04$ mag). The high-energy spectral index β_2 is tied to β_1 through $\beta_2 = \beta_1 + 0.5$ as expected for synchrotron emission (predicted by Sari et al. 1998, and observed by Greiner et al. 2011, Zafar et al. 2011, and Covino et al. 2013), and the best-fit soft X-ray absorption at $z = 5.0$ corresponds to $N(\mathrm{H})_\mathrm{X} = (1.8 \pm 0.4) \times 10^{22}\,\mathrm{cm}^{-2}$. Because of the small amount of reddening, an LMC (Large Magellanic Cloud) dust model provides a reasonable description of the optical/NIR data as well ($\chi^2 = 3.8$) and yields similar values for all parameters within the errors. A fit with a Milky Way dust model is significantly worse ($\chi^2 = 9.4$) because of the lack of a 2175 Å dust feature in our data.

5. THE INTERVENING SYSTEM AT $z = 4.6$

In the line of sight toward the afterglow of GRB 111008A an additional DLA system is detected at $z = 4.6$, with a neutral hydrogen column density of $\log N(\mathrm{H\,I})/\mathrm{cm}^{-2} = 21.34 \pm 0.10$ (Figure 1). A number of strong metal absorption lines are detected from this system, including C IV, Mg I, Mg II, Si II, Si IV, Fe II, and Ni II. We note that the $\mathrm{EW}_\mathrm{rest}$ of Si II λ1526 is the second highest ever detected for a DLA at $z > 4$ ($\mathrm{EW}_\mathrm{rest} = 2.30 \pm 0.02$ Å), indicating a relatively high metallicity for this redshift (Prochaska et al. 2008; Rafelski et al. 2012).

The low- and high-ionization lines show multiple components. Due to their saturation, we do not include the Si IV and C IV lines in our analysis. The absorption lines from singly ionized species are fitted with Voigt profiles, in which we assume that the different ions have the same velocity structure, i.e., equal z and b parameters per velocity component. In Figure 4, we show the best fit for the most constraining absorption lines, which needs five components for the strongest lines. In the Voigt profile fitting we have included more lines than shown in the figure, most of which are visually absent, but we have avoided regions with strong telluric contamination. Including both strong and weak lines, predominantly of Fe II, helps to constrain the b parameters. For the different absorption components the Voigt profile fitting results in the following b parameters (z values): 5.0 ± 27.7 km s^{-1} (4.60337 ± 0.00009), 36.4 ± 2.8 km s^{-1} (4.60611 ± 0.00004), 41.8 ± 2.9 km s^{-1} (4.60848 ± 0.00003), 45.2 ± 2.3 km s^{-1} (4.61110 ± 0.00003), and 10.7 ± 2.0 km s^{-1} (4.61337 ± 0.00002). Outside this section we will refer to the redshift of the intervening absorber as $z = 4.6$.

The total column densities of Si II, Fe II, and Ni II can be constrained and are summarized in Table 1. The column densities of Fe II and Ni II are robust because they are determined from optically thin lines. The fit for Si II is mainly determined by the saturated Si II λ1526 transition, as Si II λ1808 is in a low S/N region, so we conservatively report a 2σ lower limit of $\log N\,(\mathrm{Si\,II})/\mathrm{cm}^{-2} > 14.91$ based on the equivalent width of this line.

The conservative lower limit on the metallicity based on the equivalent width of Si II λ1526 is 1% solar. The value of [Ni/H] indicates a metallicity of 3%–6% solar, and [Fe/H] corresponds to 2%–4% solar. For QSO and GRB DLAs at these metallicities (e.g., Dessauges-Zavadsky et al. 2006; Prochaska et al. 2007b; Savaglio et al. 2003) these elements (especially Ni and Fe) are often depleted onto dust grains, which implies that the true metallicity might be (much) higher. Generally, the ratio [Zn/Fe], if available, is used to correct for dust depletion, since Zn is expected to be mainly in the gas phase even if a lot of dust is present. Unfortunately, for this intervening absorber we could not reliably constrain the column density of Zn, since Zn II λ2026 is coincident with a skyline, and Zn II λ2062 is blended with Cr II λ2062.

6. SEARCHING FOR EMISSION FROM THE HOST AND FROM THE INTERVENING ABSORBER

On the night of 2013 August 1–2, we obtained deep imaging of the field of GRB 111008A using the ESO/VLT and FORS2 (Appenzeller et al. 1998) to search for the counterparts of the host and for the intervening DLA in emission (as it has been done for, e.g., GRB 070721B; see Schulze et al. 2012). Our FORS2 observations consisted of 31 dithered exposures of 3 minutes of integration time each in the z_Gunn-band filter, which is centered around 9100 Å. The data were processed and calibrated in a similar way to the GROND imaging data (see Section 2.3). The stacked FORS2 image has an FWHM of the stellar point-spread function of 0.″9 and reaches a 2σ depth of a z-band magnitude of 26 $\mathrm{mag_{AB}}$.

We do not detect emission centered at the position of the optical transient, and we set an upper limit of $z > 25.6\,\mathrm{mag_{AB}}$ for the brightness of the GRB host galaxy by measuring the flux at the GRB position in an aperture of size of one FWHM. Especially at the highest redshifts, GRB hosts are faint (Hjorth et al. 2012; Tanvir et al. 2012), and the lack of a clear counterpart to the GRB-DLA in our imaging is thus not particularly surprising.

We detect significant emission centered at a projected distance of $0.''65 \pm 0.''15$ to the optical counterpart with an AB magnitude of $z = 25.4 \pm 0.3$. We consider this a more likely candidate for the counterpart of the intervening DLA at $z = 4.6$ than for the $z = 5.0$ host system. Also, finding an unrelated galaxy at these flux levels is not unlikely. The probability (estimated following Bloom et al. 2002) of finding a random field galaxy with $z < 25.4$ mag at this distance to the GRB is approximately 3%. An association between the detected source and the DLA could be supported or rejected from further imaging, for example. At $z = 4.6$, a galaxy is expected to show a strong Lyα break between the r and the i band and no flux transmitted below 5100 Å.

If associated with the DLA at $z = 4.6$, the FORS2 z-band measurement yields an absolute magnitude of $M_\mathrm{UV} = -20.9 \pm 0.3$ mag at a rest-frame wavelength of ∼1600 Å, typical of the brightest Lyman break galaxies at this redshift. Compared to the galaxy luminosity function, this magnitude corresponds to $\approx L_\star$ (Bouwens et al. 2007). The measured spatial offset between GRB line of sight and galaxy center would be 4 ± 1 kpc at $z = 4.6$.

Since the absorber has a high metallicity and a high velocity width, the chances are that this absorber is part of a massive galaxy (Wolfe et al. 2008). This would agree with the detection of this bright Lyman break galaxy.

7. DUST-TO-METALS RATIO

The study of the dust-to-metals ratio (DTM) as a function of metallicity holds the potential to probe the dust formation mechanism. If dust is primarily produced by SNe, the DTM is expected to be independent of metallicity (Morgan & Edmunds 2003). If dust grains grow in the ISM, a decline of the DTM is expected at low metallicities (Draine 2009; Mattsson et al. 2012; Herrera-Camus et al. 2012). The host galaxy of GRB 111008A is characterized by a variety of metal absorption lines, and the afterglow SED is well calibrated. Thus, in this line of sight we

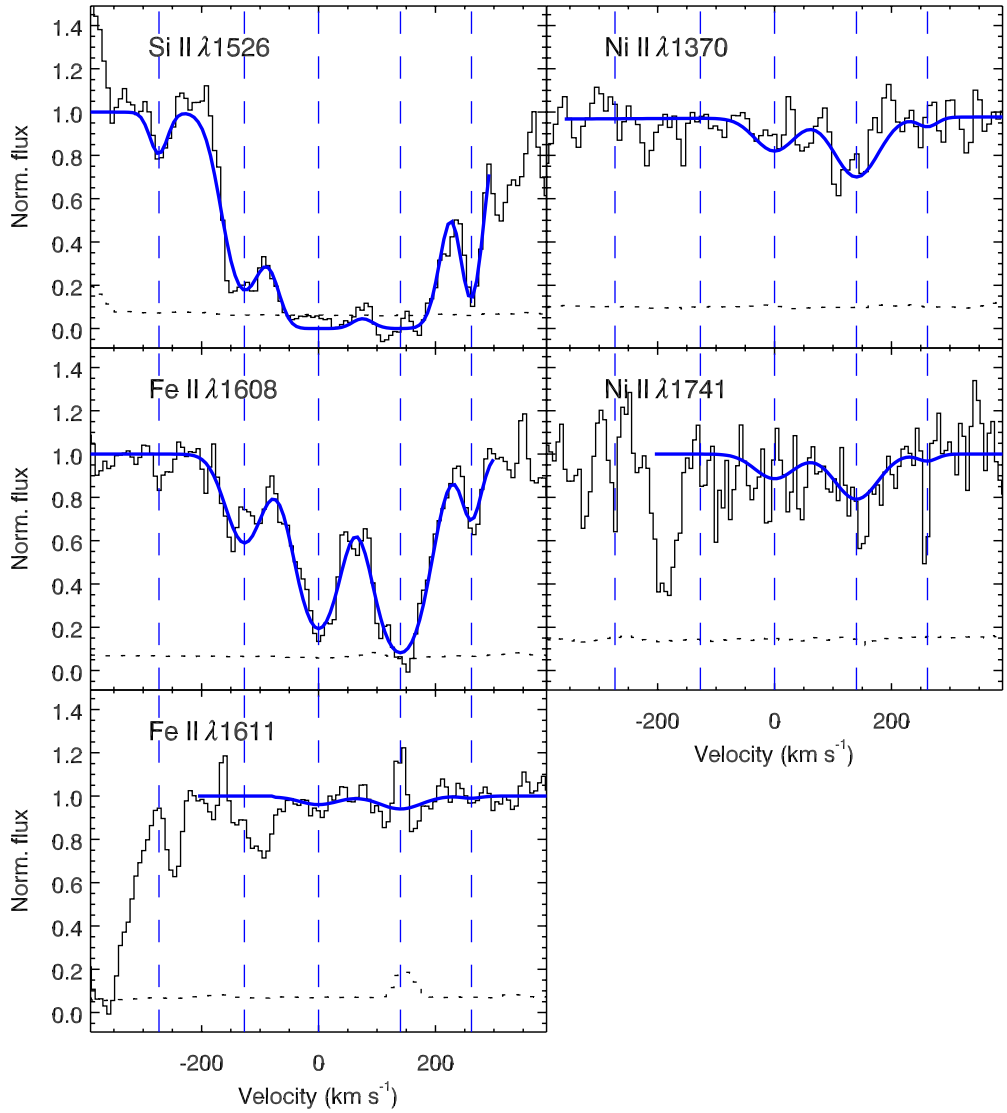

Figure 4. Most constraining metal lines from the intervening absorber at $z = 4.6$. The solid profiles are resulting Voigt-profile fits with five absorption components (the dashed vertical lines show the velocity of the absorption components). The dotted line shows the error spectrum.

(A color version of this figure is available in the online journal.)

have the opportunity to examine the question of the DTM of the GRB host galaxy through dust extinction along the line of sight.

For a system with a given extinction and metallicity we can calculate the DTM relative to the Local Group value as

$$\mathrm{DTM} = \frac{1}{\mathrm{DTM_{LG}}} \times \frac{A_V}{N_{\mathrm{H\,I}} \times 10^{[\mathrm{M/H_I}]}}, \quad (1)$$

where $\mathrm{DTM_{LG}} \equiv 10^{-21.3}$ mag cm^2 is the DTM in the Local Group (Watson 2011). Recently, Zafar & Watson (2013), using different classes of objects, found that DTM is independent of galaxy type or age, redshift, or metallicity and is very close to the value in the Local Group.

The measured extinction along the sight line of GRB 111008A is affected by the host galaxy, as well as the intervening absorber. Assuming that all the extinction is from the host galaxy and that the host galaxy has a metallicity of [M/H] = [S/H], we find that the host galaxy has

$$\mathrm{DTM} = 0.57 \pm 0.26. \quad (2)$$

We calculated the mean and the error of the DTM in a Monte Carlo fashion, where 50,000 values for A_V, $\log N_{\mathrm{H}}$, and [M/H] are drawn from normal distributions with $A_V = 0.11 \pm 0.04$ mag, $\log N_{\mathrm{H}}/\mathrm{cm}^{-2} = 22.30 \pm 0.06$, and $[\mathrm{M/H}] = -1.70 \pm 0.10$. For each triplet of sampled values a DTM is calculated, and finally the mean and the standard deviation of the 50,000 DTM values are computed.

In Figure 5 we plot the DTM versus the metallicity for the GRB 111008A host with GRB-DLAs, QSO-DLAs, nearby lensed galaxies, and with the value found in the Local Group (see Zafar & Watson 2013 and Chen et al. 2013 for details). Given the uncertainty in A_V, the host has a DTM that —within a 1σ error bar—is consistent with the DTM observed in the Local Group. Our data are also consistent with the scenario where the host has a much lower DTM than the Local Group, especially if part of the extinction along the line of sight is due to the intervening absorber at $z = 4.6$.

8. DISCUSSION

8.1. The GRB Host Galaxy

The abundance analysis shows that the GRB host absorber is a relatively low metallicity system (about 2% solar metallicity)

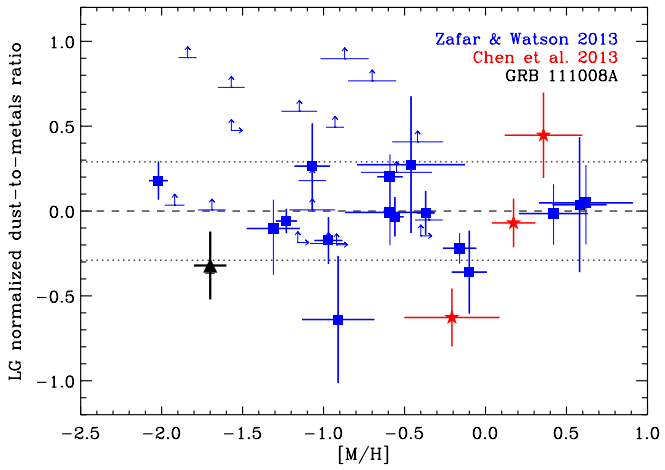

Figure 5. Dust-to-metals ratio vs. metallicity. The dashed line shows the Local Group value, and the dotted lines indicate the scatter in the Local Group. The host of GRB 111008A, which is shown as a black triangle, has a dust-to-metals ratio that is consistent with being equal to or lower than the value in the Local Group. The other data points are from Zafar & Watson (2013) and Chen et al. (2013).

(A color version of this figure is available in the online journal.)

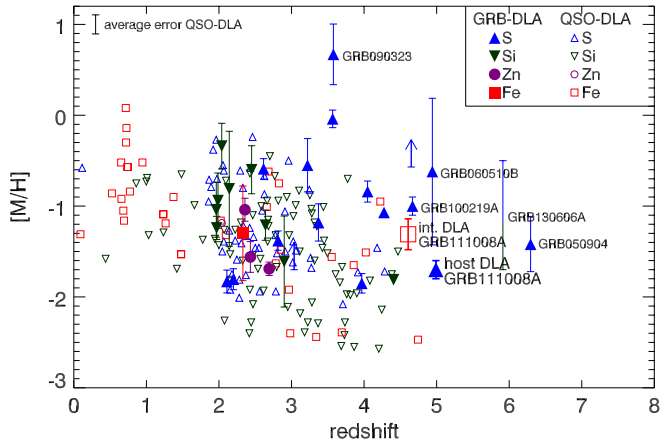

Figure 6. Absorption-line-based metallicities [M/H] as a function of redshift for GRB-DLAs (filled symbols) and QSO-DLAs (open symbols). The figure is adapted from Rafelski et al. (2012), with added GRB-DLAs from the following references: Savaglio et al. (2003), Vreeswijk et al. (2004), Fiore et al. (2005), Kawai et al. (2006), Watson et al. (2006), Berger et al. (2006), Prochaska et al. (2007a), Price et al. (2007), Chary et al. (2007), Thöne et al. (2008), Prochaska et al. (2009), D'Avanzo et al. (2010), D'Elia et al. (2010), Schady et al. (2011), De Cia et al. (2011), D'Elia et al. (2012), Thöne et al. (2013), Krühler et al. (2013), Chornock et al. (2013), and D'Elia et al. (2014). (For the measurement of the metallicity of GRB 130606A from Chornock et al. 2013, the lower limit is based on Si and the upper limit is based on S. We have indicated this by the colors of the error bar belonging to this data point.) Following Rafelski et al. (2012), we apply [M/H] = [Fe/H] + 0.3 in cases where the metal is iron, and no less refractory element abundance is measured (this correction is also applied to the intervening absorber in the GRB 111008A sight line).

(A color version of this figure is available in the online journal.)

compared to the other GRB-DLAs at $z > 4.5$ (GRB 100219A and GRB 050904); see Figure 6. The relative abundances are close to solar, as shown in Table 1, but we are unable to address whether the metals are depleted onto dust grains, since we have no reliable measurement of [Zn/Fe] (typically decreasing with metallicity in both QSO- and GRB-DLAs; Wolfe et al. 2005; Savaglio et al. 2003; Dessauges-Zavadsky et al. 2006; Prochaska et al. 2007b; Noterdaeme et al. 2008; Rafelski et al. 2012), which is normally used to determine the amount of dust depletion.

In Figure 7, the two high-z GRBs 100219A and 111008A (i.e., the only two GRBs with $z > 4.7$ and measured metallicities

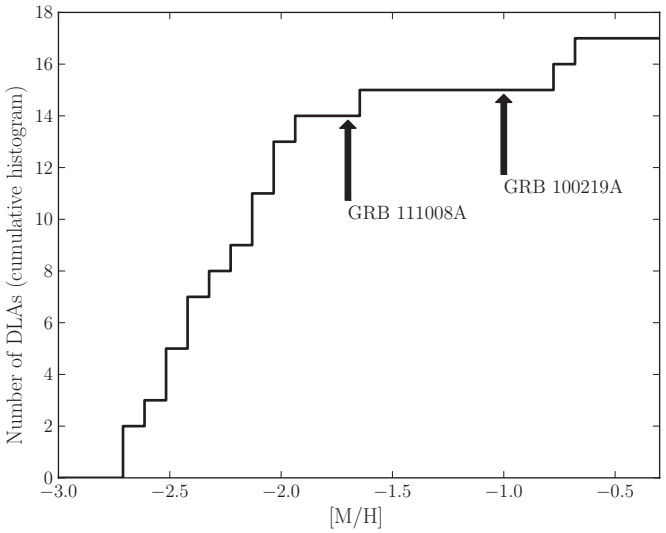

Figure 7. Figure compares the metallicity of the two high-redshift GRBs 100219A and 111008A with the 17 QSO-DLAs at $3.64 < z < 5.08$ from Rafelski et al. (2014). The two GRB-DLAs are clearly in the upper part of the metallicity distribution of QSO-DLAs, a trend that is also present at lower redshift.

with errors smaller than 0.5 dex) are compared to the recently measured QSO-DLA metallicities (from Rafelski et al. 2014) at similar redshifts. The GRB metallicities fall within the range spanned by QSO-DLAs, but typically in the upper end of the distribution. This trend is also present at lower redshift (Fynbo et al. 2008). This phenomenon can be explained by the fact that GRB afterglows generally probe the star-forming "hearts" of galaxies, while QSO-DLAs have a higher chance to probe the (less metal-rich) outskirts of galaxies (see, e.g., Prochaska et al. 2007b; Lemasle et al. 2013). It is remarkable, however, that the metallicity of GRB-DLAs does not seem to be as redshift dependent as the metallicity of QSO-DLAs. At lower redshifts the H I column density of GRB absorbers is much larger than that of QSO-DLAs.

Concerning α-element overabundance, Rafelski et al. (2012) argue that the α-to-iron-group abundance ratios in QSO-DLAs are consistent with those of halo stars in the Milky Way. Unfortunately, with the lack of a reliably determined column density of zinc, we cannot distinguish the scenario where dust depletion and α-element overabundance both are present from the scenario where α-element overabundance and dust depletion both are absent.

The afterglow spectrum of the high-redshift GRB 100219A ($z = 4.7$) studied by Thöne et al. (2013) reveals a substantially higher metallicity of $[M/H] = -1.0 \pm 0.1$ and evidence for either depletion on dust grains or a strong α-element overabundance ($[S/Fe] = 0.8$). The GRB 100219A absorber is also substantially more complex with five velocity components spread over 160 km s^{-1}, whereas we only require two components separated by 70 km s^{-1} to fit the metal lines from the GRB 111008A absorber. Higher velocity widths for GRB 100219A compared to GRB 111008A are also expected due to the relation between velocity width and metallicity (Ledoux et al. 2006; Neeleman et al. 2013).

The study by Rafelski et al. (2014) measures metallicities of 17 QSO-DLAs with $z = 3.64$–5.08. They show that the metallicity of QSO-DLAs decreases rapidly at $z > 4.7$, likely because the state of the gas in the outer part of DLA galaxies changes at this redshift. It is unknown whether GRB-DLAs

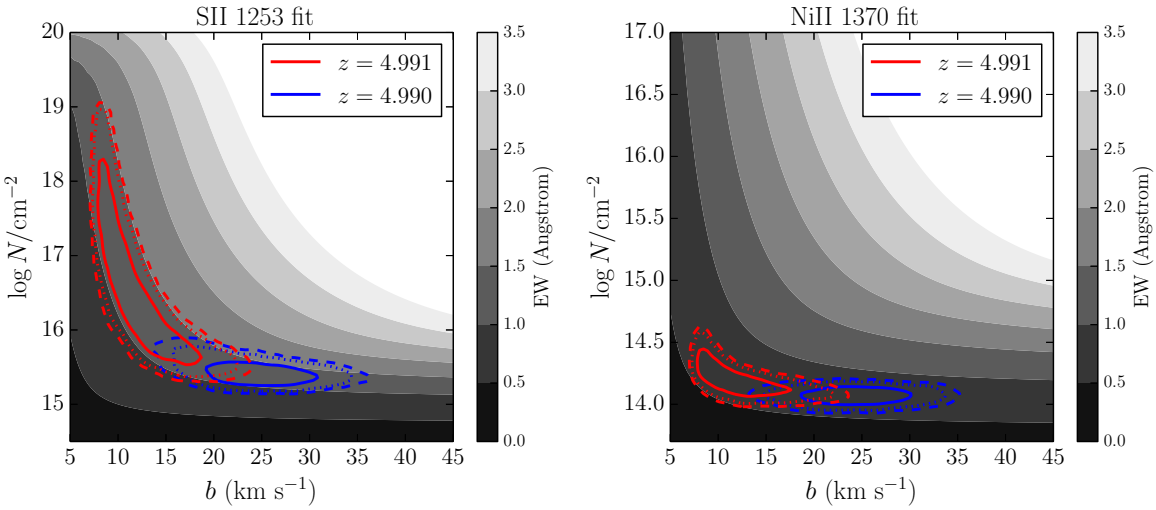

Figure 8. 1σ, 2σ, and 3σ confidence levels (solid, dotted, and dashed contours, respectively) for the Doppler parameters and the column densities for S II and Ni II. The gray contours show regions of constant equivalent width.

(A color version of this figure is available in the online journal.)

exhibit the same trend. So far the only GRB-DLAs with a well-determined metallicity at $z > 4.7$ are GRB 111008A and GRB 100219A. Since GRB-DLA sight lines have a different origin than QSO-DLAs, it is not evident whether or not a similar decline in the metallicity of GRB-DLAs is present.

8.2. The Intervening DLA

The $z = 4.6$ intervening DLA absorber has a high neutral hydrogen column density, which is consistent with being among the highest column densities of the 18 QSO-DLAs observed at similar high redshifts by Rafelski et al. (2014). A high metallicity is also indicated by the large equivalent width of Si II λ1526. This suggests that this is not a typical intervening system likely associated with the outer regions of the absorber (Prochaska et al. 2007b). It is possible that the line of sight toward the GRB crossed inner parts of the foreground absorber, thus showing higher column densities and metallicity. Further observations can potentially reveal the nature of the intervening absorber.

9. SUMMARY

With spectroscopy of the GRB 111008A afterglow, we have a rare chance of studying the properties of a sight line originating in a star-forming region of a $z = 5.0$ galaxy. By analyzing absorption lines from the ISM of the GRB's host galaxy, a metallicity of [S/H] $= -1.70 \pm 0.10$ is measured, and from fitting the SED the dust extinction is determined to be $A_V = 0.11 \pm 0.04$ mag. The DTM is equal to or lower than what is observed in the Local Group. Determination of the DTM of such high-redshift environments is important, since it can potentially constrain dust production mechanisms.

GRB 111008A offers two noteworthy features: it is the highest-redshift GRB host galaxy with such a precise metallicity measurement, and it is also the first time fine-structure lines from Fe II have been observed at such a high redshift. This is special because the S/N required to detect the relatively weak fine-structure lines is often not reached at high redshift. Their presence unambiguously confirms the absorption system as the GRB's host galaxy.

In the sight line toward the GRB is also a DLA at $z = 4.6$. The metallicity of this system is constrained by [Si/H] > -2.15 at a 2σ limit, [Fe/H] $= -1.61 \pm 0.17$ and [Ni/H] $= -1.33 \pm 0.12$. The role of dust depletion is unclear. With photometric observations of the field surrounding the GRB's position performed roughly two years after explosion, we detect emission from a source, which could be the intervening system. The offset between the detected source and the GRB sight line would be 4 ± 1 kpc at the redshift of the intervening DLA. Deeper observations could potentially reveal whether or not this source is related to the intervening DLA at $z = 4.6$.

We thank the referee for very useful comments. We also thank A. De Cia for useful comments and discussions. The Dark Cosmology Centre is funded by the DNRF. This research is partly based on observations obtained at the Gemini Observatory, which is operated by the Association of Universities for Research in Astronomy, Inc., under a cooperative agreement with the NSF on behalf of the Gemini partnership. O.E.H. acknowledges the Dutch Research School for Astronomy (NOVA) for a PhD grant. T.K. acknowledges support by the European Commission under the Marie Curie Intra-European Fellowship Programme in FP7. J.P.U.F. and B.M.J. acknowledge support from the ERC-StG grant EGGS-278202. Part of the funding for GROND (both hardware and personnel) was generously granted from the Leibniz-Prize to Prof. G. Hasinger (DFG grant HA 1850/28-1). S.K. acknowledges support by DFG grant Kl 766/16-1, and M.N. by DFG grant SA 2001/2-1. S.S. acknowledges support from the Iniciativa Cientifica Milenio grant P10-064-F (Millennium Center for Supernova Science), with input from "Fondo de Innovación para la Competitividad, del Ministerio de Economía, Fomento y Turismo de Chile," and Basal-CATA (PFB-06/2007).

APPENDIX A

THE ISSUE OF SATURATION FOR THE S II λ1253 TRANSITION

In Section 3.1, it is mentioned that the S II λ1253 transition is mildly saturated. To clearly address the issue of saturation for this transition, we developed a multi-component line fitting code, where the Monte Carlo Markov Chain (MCMC) package, *Emcee* (Foreman-Mackey et al. 2013), is used as the fitting method. Such MCMC algorithms are ideal for cases with

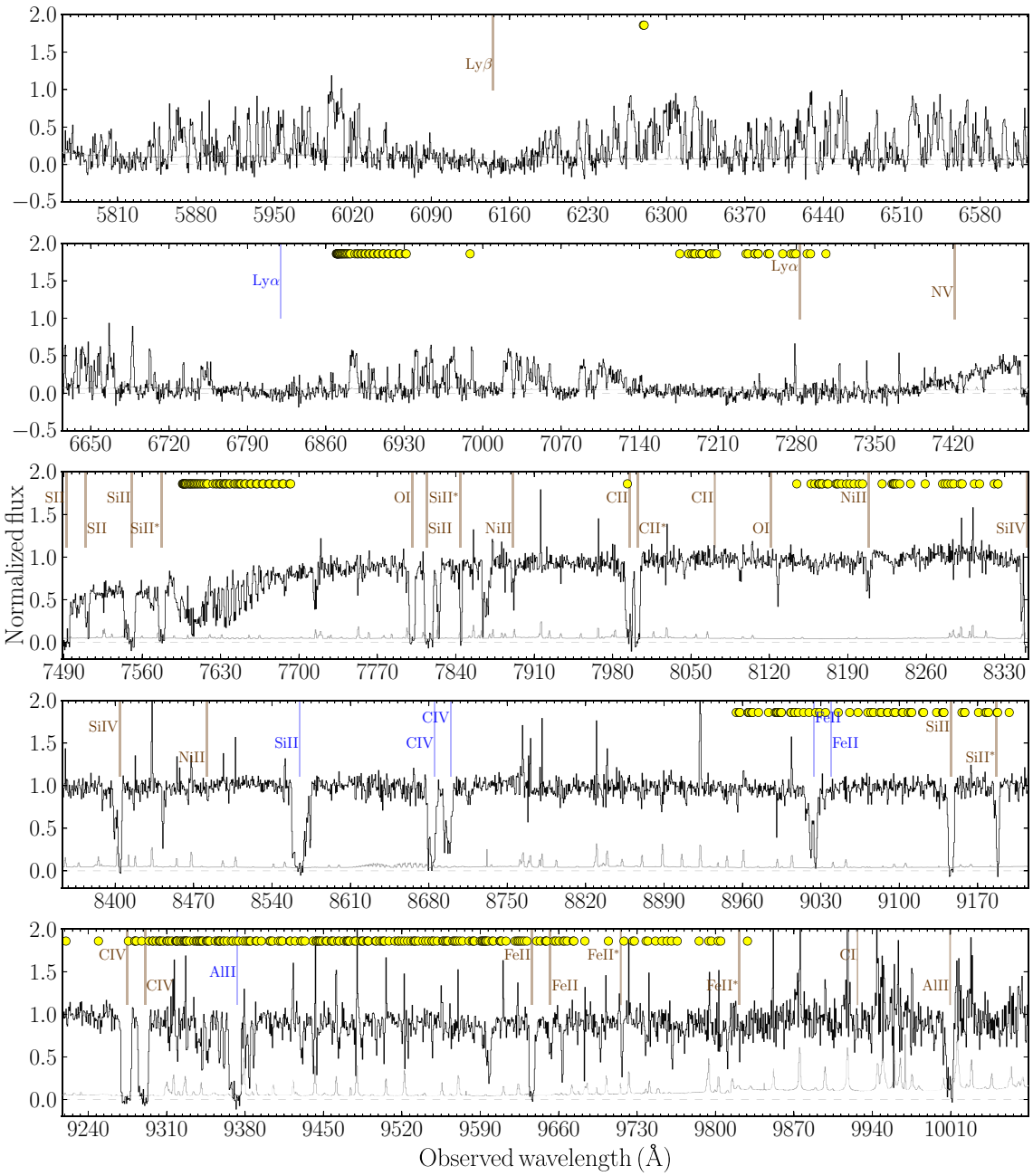

Figure 9. VIS spectrum. The yellow circles mark telluric features, the brown marks show absorption lines from the GRB host galaxy, and the blue marks show absorption features from the intervening system at $z = 4.6$. The spectrum is shown in black and the error spectrum is shown in gray.

(A color version of this figure is available in the online journal.)

degenerate models. A fit is performed for Ni II λ1370 and S II λ1253. In the MCMC run we use a flat prior with $8 < b(\mathrm{km\ s^{-1}}) < 40$ and $12 < \log N/\mathrm{cm^{-2}} < 19$ for both S and Ni. Again, we use two absorption components for each transition, and the b and z values are linked between Ni II λ1370 and S II λ1253. We sample 96,000 points from the likelihood function after a burn-in of 32,000 points (to ensure convergence of the chain).

In Figure 8, the 1σ, 2σ, and 3σ contours are shown for the b and N values, as well as contours of constant equivalent width. For Ni II λ1370 the column density is well constrained for both components.[26] For S II λ1253, the blue component has a well-constrained column density, whereas the red component is saturated (the column density can vary by four orders of magnitude within the 2σ confidence interval).

For Ni II λ1370, the difference in $\log N$ for the two components is relatively small (for the blue component $\log N/\mathrm{cm^{-2}}$ is only 0.1 dex lower than for the red component). Assuming the same difference in $\log N/\mathrm{cm^{-2}}$ for the two components of S II λ1253, we derive $\log N/\mathrm{cm^{-2}} = 15.79 \pm 0.08$, which is clearly consistent with the value reported in Table 1. Thus, the column density of S II can be reliably determined even though one of the components is saturated.

Finally, we note that the blue component has a larger b value than the red component in the model in the present section. This is contradicting the results from Section 3.1, where the red component has a larger b value than the blue component.

[26] Note that here the contribution from fine-structure lines is not included in the column density of nickel (unlike in Table 1, where it is included).

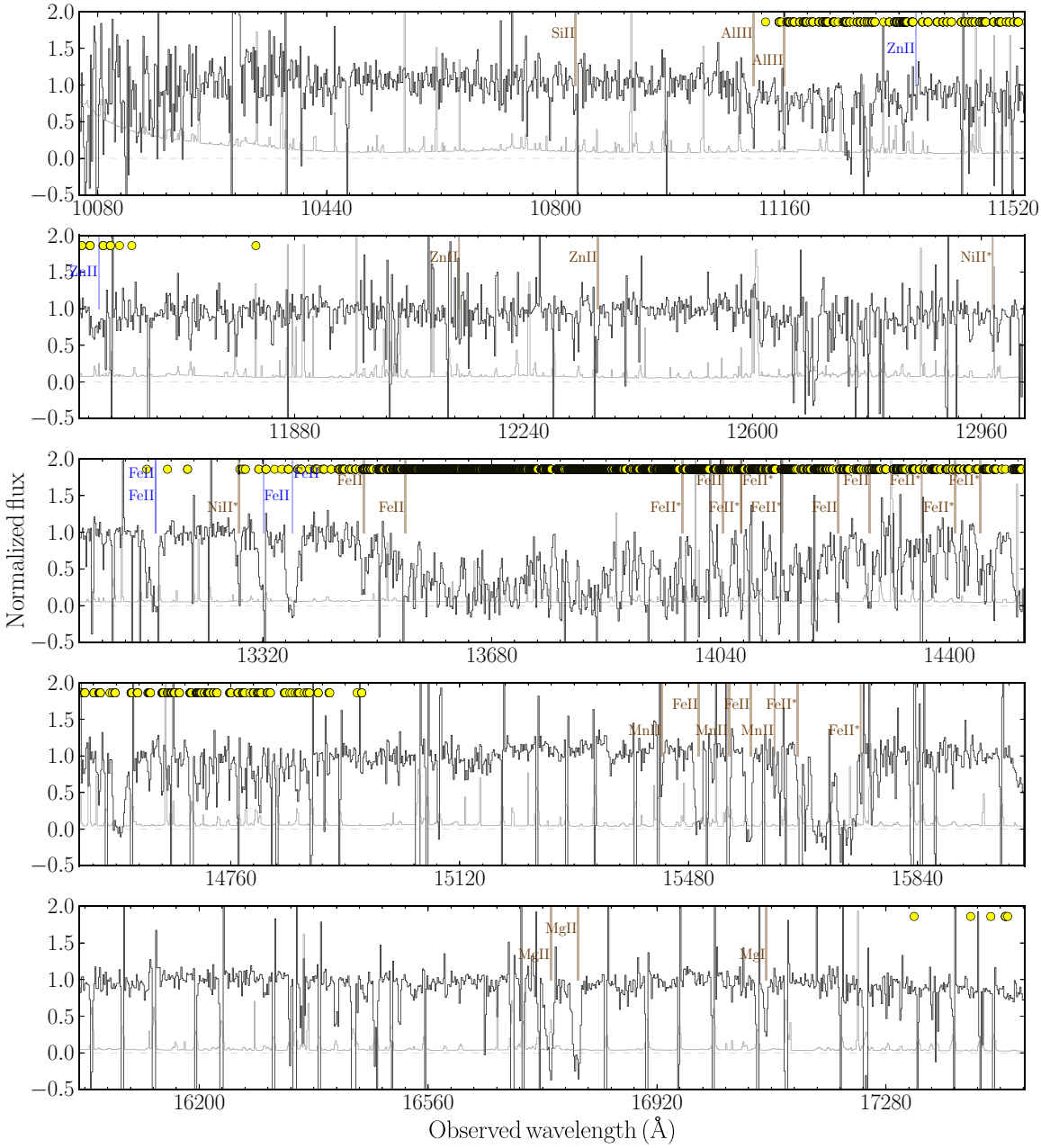

Figure 10. Same as Figure 9, but for the NIR spectrum.
(A color version of this figure is available in the online journal.)

The explanation is that more absorption lines are included in the model in Section 3.1. If we remove all other absorption components than S II and Ni II from the model in Section 3.1, we get $b = 22.8 \pm 4.0$ km s^{-1} for the blue component and $b = 15.6 \pm 4.3$ km s^{-1} for the red component, which is consistent with the b values from the present section. In all cases (i.e., in the MCMC model and in the two VPFIT models) we obtain column densities that are consistent with each other, so this is not an important caveat.

A.1. The Effect of a Third Absorption Component

An assumption in the above derivation of the sulfur column density is that there are only two absorption components. We will now discuss how a third hidden component would affect the derived column density of sulfur. The red component of S II λ1253 is mildly saturated, and it would therefore be possible to add a narrow line with the same redshift as the red component without affecting the way the spectrum looks. We could, for example, add an extra component with $b = 10$ km s^{-1} and $\log N/\mathrm{cm}^{-2} = 16.3$ without affecting the spectrum, if the component has a redshift coinciding with the red component.

The blue component is not saturated, so here it is not possible to add such a component without heavily modifying the spectrum. The situation is therefore the same as in Figure 8; the blue component is reliably determined, and the red component is uncertain because it is saturated, so we can only derive the total column density under the assumption that the ratio between the column density of the blue and the red component is the same as for nickel. Our conclusion is that the probability that large column densities are present in a hidden saturated component is low.

APPENDIX B

THE X-SHOOTER SPECTRUM

Figures 9 and 10 show absorption lines in the normalized X-shooter spectrum for the VIS and NIR arms.

REFERENCES

Aihara, H., Allende Prieto, C., An, D., et al. 2011, ApJS, 193, 29
Appenzeller, I., Fricke, K., Fürtig, W., et al. 1998, Msngr, 94, 1
Asplund, M., Grevesse, N., Sauval, A. J., & Scott, P. 2009, ARA&A, 47, 481
Basa, S., Cuby, J. G., Savaglio, S., et al. 2012, A&A, 542, A103
Baumgartner, W. H., Barthelmy, S. D., Cummings, J. R., et al. 2011, GCN, 12424, 1
Beardmore, A. P., Evans, P. A., Goad, M. R., & Osborne, J. P. 2011, GCN, 12425, 1
Berger, E., Chornock, R., Holmes, T. R., et al. 2011, ApJ, 743, 204
Berger, E., Penprase, B. E., Cenko, S. B., et al. 2006, ApJ, 642, 979
Bloom, J. S., Kulkarni, S. R., & Djorgovski, S. G. 2002, AJ, 123, 1111
Bouwens, R. J., Illingworth, G. D., Franx, M., & Ford, H. 2007, ApJ, 670, 928
Campana, S., Mangano, V., Blustin, A. J., et al. 2006, Natur, 442, 1008
Chary, R., Berger, E., & Cowie, L. 2007, ApJ, 671, 272
Chen, B., Dai, X., Kochanek, C. S., & Chartas, G. 2013, arXiv:1306.0008
Chornock, R., Berger, E., Fox, D. B., et al. 2013, ApJ, 774, 26
Covino, S., Melandri, A., Salvaterra, R., et al. 2013, MNRAS, 432, 1231
Cucchiara, A., Levan, A. J., Fox, D. B., et al. 2011, ApJ, 736, 7
D'Avanzo, P., Perri, M., Fugazza, D., et al. 2010, A&A, 522, A20
De Cia, A., Jakobsson, P., Björnsson, G., et al. 2011, MNRAS, 412, 2229
D'Elia, V., Campana, S., Covino, S., et al. 2012, MSAIS, 21, 206
D'Elia, V., Fynbo, J. P. U., Covino, S., et al. 2010, A&A, 523, A36
D'Elia, V., Fynbo, J. P. U., Goldoni, P., et al. 2014, arXiv:1402.4026
Dessauges-Zavadsky, M., Prochaska, J. X., D'Odorico, S., Calura, F., & Matteucci, F. 2006, A&A, 445, 93
Draine, B. T. 2009, in ASP Conf. Ser. 414, Cosmic Dust—Near and Far, ed. T. Henning, E. Grün, & J. Steinacker (San Francisco, CA: ASP), 453
Evans, P. A., Beardmore, A. P., Page, K. L., et al. 2007, A&A, 469, 379
Evans, P. A., Beardmore, A. P., Page, K. L., et al. 2009, MNRAS, 397, 1177
Fiore, F., D'Elia, V., Lazzati, D., et al. 2005, ApJ, 624, 853
Foreman-Mackey, D., Hogg, D. W., Lang, D., & Goodman, J. 2013, PASP, 125, 306
Fynbo, J. P. U., Jakobsson, P., Prochaska, J. X., et al. 2009, ApJS, 185, 526
Fynbo, J. P. U., Prochaska, J. X., Sommer-Larsen, J., Dessauges-Zavadsky, M., & Møller, P. 2008, ApJ, 683, 321
Fynbo, J. P. U., Starling, R. L. C., Ledoux, C., et al. 2006, A&A, 451, L47
Galama, T. J., Vreeswijk, P. M., van Paradijs, J., et al. 1998, Natur, 395, 670
Greiner, J., Bornemann, W., Clemens, C., et al. 2008, PASP, 120, 405
Greiner, J., Krhler, T., Klose, S., et al. 2011, A&A, 526, A30
Hartoog, O. E., Wiersema, K., Vreeswijk, P. M., et al. 2013, MNRAS, 430, 2739
Herrera-Camus, R., Fisher, D. B., Bolatto, A. D., et al. 2012, ApJ, 752, 112
Hjorth, J., & Bloom, J. S. 2012, The Gamma-Ray Burst—Supernova Connection (Cambridge: Cambridge Univ. Press), 169
Hjorth, J., Malesani, D., Jakobsson, P., et al. 2012, ApJ, 756, 187
Hjorth, J., Sollerman, J., Møller, P., et al. 2003, Natur, 423, 847
Horne, K. 1986, PASP, 98, 609
Jakobsson, P., Hjorth, J., Fynbo, J. P. U., et al. 2004, ApJL, 617, L21
Kalberla, P. M. W., Burton, W. B., Hartmann, D., et al. 2005, A&A, 440, 775
Kawai, N., Kosugi, G., Aoki, K., et al. 2006, Natur, 440, 184
Krühler, T., Greiner, J., Schady, P., et al. 2011, A&A, 534, A108
Krühler, T., Küpcü Yoldaş, A., Greiner, J., et al. 2008, ApJ, 685, 376
Krühler, T., Ledoux, C., Fynbo, J. P. U., et al. 2013, A&A, 557, A18
Ledoux, C., Petitjean, P., Fynbo, J. P. U., Møller, P., & Srianand, R. 2006, A&A, 457, 71
Ledoux, C., Vreeswijk, P. M., Smette, A., et al. 2009, A&A, 506, 661
Lemasle, B., François, P., Genovali, K., et al. 2013, A&A, 558, A31
Levan, A. J., Wiersema, K., & Tanvir, N. R. 2011a, GCN, 12426, 1
Levan, A. J., Wiersema, K., & Tanvir, N. R. 2011b, GCN, 12429, 1
Matteucci, F., & Greggio, L. 1986, A&A, 154, 279
Mattsson, L., Andersen, A. C., & Munkhammar, J. D. 2012, MNRAS, 423, 26
Modigliani, A., Goldoni, P., Royer, F., et al. 2010, Proc. SPIE, 7737, 56
Modjaz, M., Stanek, K. Z., Garnavich, P. M., et al. 2006, ApJL, 645, L21
Morgan, H. L., & Edmunds, M. G. 2003, MNRAS, 343, 427
Nardini, M., Klose, S., Greiner, J., & Afonso, P. 2011, GCN, 12428, 1
Neeleman, M., Wolfe, A. M., Prochaska, J. X., & Rafelski, M. 2013, ApJ, 769, 54
Noterdaeme, P., Ledoux, C., Petitjean, P., & Srianand, R. 2008, A&A, 481, 327
Pei, Y. C. 1992, ApJ, 395, 130
Perley, D. A., Cenko, S. B., Bloom, J. S., et al. 2009, AJ, 138, 1690
Price, P. A., Songaila, A., Cowie, L. L., et al. 2007, ApJL, 663, L57
Prochaska, J. X., Chen, H.-W., & Bloom, J. S. 2006, ApJ, 648, 95
Prochaska, J. X., Chen, H.-W., Bloom, J. S., et al. 2007a, ApJS, 168, 231
Prochaska, J. X., Chen, H.-W., Dessauges-Zavadsky, M., & Bloom, J. S. 2007b, ApJ, 666, 267
Prochaska, J. X., Chen, H.-W., Wolfe, A. M., Dessauges-Zavadsky, M., & Bloom, J. S. 2008, ApJ, 672, 59
Prochaska, J. X., Sheffer, Y., Perley, D. A., et al. 2009, ApJL, 691, L27
Rafelski, M., Neeleman, M., Fumagalli, M., Wolfe, A. M., & Prochaska, J. X. 2014, ApJL, 782, L29
Rafelski, M., Wolfe, A. M., Prochaska, J. X., Neeleman, M., & Mendez, A. J. 2012, ApJ, 755, 89
Salvaterra, R., Della Valle, M., Campana, S., et al. 2009, Natur, 461, 1258
Sari, R., Piran, T., & Narayan, R. 1998, ApJL, 497, L17
Savaglio, S. 2006, NJPh, 8, 195
Savaglio, S., Fall, S. M., & Fiore, F. 2003, ApJ, 585, 638
Saxton, C. J., Barthelmy, S. D., Beardmore, A. P., et al. 2011, GCN, 12423, 1
Schady, P., Savaglio, S., Krühler, T., Greiner, J., & Rau, A. 2011, A&A, 525, A113
Schulze, S., Fynbo, J. P. U., Milvang-Jensen, B., et al. 2012, A&A, 546, A20
Skrutskie, M. F., Cutri, R. M., Stiening, R., et al. 2006, AJ, 131, 1163
Sparre, M., Sollerman, J., Fynbo, J. P. U., et al. 2011, ApJL, 735, L24
Stanek, K. Z., Matheson, T., Garnavich, P. M., et al. 2003, ApJL, 591, L17
Tanvir, N. R., Fox, D. B., Levan, A. J., et al. 2009, Natur, 461, 1254
Tanvir, N. R., Levan, A. J., Fruchter, A. S., et al. 2012, ApJ, 754, 46
Thöne, C. C., Fynbo, J. P. U., Goldoni, P., et al. 2013, MNRAS, 428, 3590
Thöne, C. C., Wiersema, K., Ledoux, C., et al. 2008, A&A, 489, 37
Tolstoy, E. 2011, Sci, 333, 176
Vernet, J., Dekker, H., D'Odorico, S., et al. 2011, A&A, 536, A105
Vreeswijk, P. M., Ellison, S. L., Ledoux, C., et al. 2004, A&A, 419, 927
Vreeswijk, P. M., Ledoux, C., Smette, A., et al. 2007, A&A, 468, 83
Watson, D. 2011, A&A, 533, A16
Watson, D., Fynbo, J. P. U., Ledoux, C., et al. 2006, ApJ, 652, 1011
Wiersema, K., Flores, H., D'Elia, V., et al. 2011, GCN, 12431, 1
Willingale, R., Starling, R. L. C., Beardmore, A. P., Tanvir, N. R., & O'Brien, P. T. 2013, MNRAS, 431, 394
Wolfe, A. M., Gawiser, E., & Prochaska, J. X. 2005, ARA&A, 43, 861
Wolfe, A. M., Prochaska, J. X., Jorgenson, R. A., & Rafelski, M. 2008, ApJ, 681, 881
Xu, D., de Ugarte Postigo, A., Leloudas, G., et al. 2013, ApJ, 776, 98
Xu, D., Malesani, D., Buchhave, L. A., Schulze, S., & Jakobsson, P. 2011, GCN, 12427, 1
Zafar, T., & Watson, D. 2013, A&A, 560, A26
Zafar, T., Watson, D., Fynbo, J. P. U., et al. 2011, A&A, 532, A143